

Kinetic magnetism and stripe order in the antiferromagnetic bosonic $t - J$ model

Timothy J. Harris ^{1,2,*}, Ulrich Schollwöck ^{1,2}, Annabelle Bohrdt ^{2,3} and Fabian Grusdt ^{1,2,†}

¹*Department of Physics and Arnold Sommerfeld Center for Theoretical Physics (ASC),
Ludwig-Maximilians-Universität München, Theresienstr. 37, München D-80333, Germany*

²*Munich Center for Quantum Science and Technology (MCQST), Schellingstr. 4, München D-80799, Germany*

³*University of Regensburg, Universitätsstr. 31, Regensburg D-93053, Germany*

(Dated: December 4, 2024)

Unraveling the microscopic mechanisms governing the physics of doped quantum magnets is key to advancing our understanding of strongly correlated quantum matter. Quantum simulation platforms, e.g., ultracold atoms in optical lattices or tweezer arrays, provide a powerful tool to investigate the interplay between spin and charge motion in microscopic detail. Here, in a new twist, we disentangle the role of particle statistics from the physics of strong correlations by exploring the strong coupling limit of doped *bosonic* quantum magnets, specifically the antiferromagnetic (AFM) bosonic $t - J$ model. Using large-scale density matrix renormalization group (DMRG) calculations, we map out the phase diagram on the 2D square lattice at finite doping. In the low-doping regime, bosonic holes form partially-filled stripes, akin to those observed in high- T_c cuprates. As doping increases, a transition occurs to a partially-polarized ferromagnetic (FM) phase, driven by the motion of mobile bosonic charge carriers forming Nagaoka polarons. At high doping or large t/J , the system evolves into a fully-polarized ferromagnet. These findings shed new light on the role of particle statistics in strongly correlated many-body systems, revealing connections to stripe formation and the physics of kinetic (i.e., Nagaoka-type) ferromagnetism. Our results may be realized in state-of-the-art quantum simulation platforms with bosonic quantum gas microscopes and Rydberg atom tweezer arrays, paving the way for future experimental studies of doped bosonic quantum magnets.

Introduction.—Developing a precise theoretical description of the complex interplay between spin and charge degrees-of-freedom in doped Mott insulators is a central challenge in strongly correlated many-body physics [1]. To date, the majority of the theoretical discussions have focussed on two paradigmatic Hamiltonians—namely the two-dimensional (2D) Fermi-Hubbard and related $t - J$ models—which are believed to capture the essential low-energy physics of high- T_c cuprate superconductors [2, 3]. While these models have been pivotal in advancing our understanding of the rich variety of intertwined phases [4], e.g., through impressive recent progress in large-scale numerical simulations [5–7], it currently remains unclear to what extent the fermionic nature of the underlying charge carriers drives the emergence of these phases, as opposed to the competition between motional and magnetic degrees-of-freedom [8]. Addressing this distinction is crucial for uncovering the mechanisms underlying high- T_c superconductivity and related phases, as it disentangles the role of particle statistics from the intrinsic physics of strong correlations.

In this context, analog quantum simulation platforms, e.g., ultracold atoms trapped in optical lattices or tweezer arrays, provide a powerful approach to exploring the role of particle statistics in the formation of striped and superconducting phases [9–11]. These systems provide well-isolated and fully-tunable realizations of minimal condensed matter models, allowing experiments to systematically probe the physics of strongly correlated ultracold quantum matter in microscopic detail [12–14]. Key advantages of these platforms include precise control over particle statistics, lattice geometry, doping

and interactions, as well as high-fidelity state preparation and measurement protocols facilitated by spin and charge resolved detection and addressing techniques [15–20]. When combined with quantum gas microscopes [9, 21, 22], these simulators enable the measurement of multi-point correlation functions that go beyond the capabilities of traditional solid-state experiments [23–27].

Building on this approach, here we study the antiferromagnetic (AFM) *bosonic* $t - J$ model, which describes the interplay of magnetic and motional degrees-of-freedom in a system of mobile bosonic holes with local AFM interactions. This model offers a unique opportunity to examine the impact of bosonic statistics in a setting similar to that of fermionic models. Moreover, the AFM bosonic $t - J$ model can be realized in systems of ultracold atoms [28], polar molecules [29–31], and Rydberg tweezer arrays [31], making it an experimentally accessible platform for testing theoretical predictions.

Previous theoretical studies of the bosonic $t - J$ model have been restricted to lower-dimensional systems, cases with only *partial* AFM couplings (e.g., $J_z > 0, J_\perp \leq 0$), or in the high-temperature regime [32–39]. However, the low-temperature (ground state) phase diagram at strong coupling ($t/J \gg 1$) with fully AFM spin-exchange interactions remains largely unexplored, particularly in the numerically challenging *finite doping* regime.

In this work, we establish the $T = 0$ phase diagram of the AFM bosonic $t - J$ model on the 2D square lattice at finite doping using large-scale density matrix renormalization group (DMRG) calculations [40–44] on finite-size cylinders [45]. At low doping, i.e., close to the Heisenberg AFM—where the ground state is independent of the un-

derlying statistics of the charge carriers—our numerical simulations unveil signatures of stripe order associated with incommensurate AFM correlations, reminiscent of the physics of doped fermionic Hubbard and $t - J$ models [46–48], establishing a connection between our results and the broader physics of doped Mott insulators. In this regime, the ground state remains a total spin-singlet.

Beyond a critical doping value, $\delta > \delta_{\text{PP}}^*$, the interplay between Heisenberg-type AFM superexchange interactions and itinerant Nagaoka-type ferromagnetism (FM), mediated by the motion of mobile bosonic holes, drives a transition to a partially-polarized (PP) FM phase, signified by a departure from a spin-singlet ground state. This transition is accompanied by the formation of so-called *Nagaoka polarons*—i.e., regions of enhanced FM correlations embedded in an otherwise AFM spin background—resulting in a strong suppression of local AFM correlations as we dope away from half-filling. These Nagaoka polarons are a hallmark of the competition between spin and charge degrees-of-freedom in strongly correlated systems and directly connect our results to the physics of kinetic (i.e., Nagaoka-type) ferromagnetism [49] recently explored in quantum simulations of the triangular lattice Hubbard model using ultracold fermions [50, 51], arrays of quantum dots [52] and moiré heterostructures [53–55].

In the limit of large doping (i.e., for dilute systems) or for large t/J , spatially overlapping Nagaoka polarons begin to percolate throughout the system, leading to the formation of a fully-polarized long-range SU(2) ferromagnetic ground state for $\delta > \delta_{\text{FM}}^*$ [51, 56]. Our results are summarized in Fig. 1.

The model.—We consider a model of two-component (i.e., spin-1/2) hard-core bosons on the 2D square lattice:

$$\begin{aligned} \hat{\mathcal{H}}_{t-J} = & -t \sum_{\langle \mathbf{i}, \mathbf{j} \rangle} \sum_{\sigma} \hat{\mathcal{P}}_G \left(\hat{a}_{\mathbf{i}\sigma}^{\dagger} \hat{a}_{\mathbf{j}\sigma} + \text{H.c.} \right) \hat{\mathcal{P}}_G \\ & + J \sum_{\langle \mathbf{i}, \mathbf{j} \rangle} \left(\hat{\mathbf{S}}_{\mathbf{i}} \cdot \hat{\mathbf{S}}_{\mathbf{j}} + \frac{3}{4} \hat{n}_{\mathbf{i}} \hat{n}_{\mathbf{j}} \right), \end{aligned} \quad (1)$$

where $\hat{a}_{\mathbf{i}\sigma}^{\dagger}$ ($\hat{a}_{\mathbf{i}\sigma}$) are the creation (annihilation) operators for a boson on lattice site $\mathbf{i} = (i_x, i_y)$ in spin state $\sigma = \uparrow, \downarrow$; $\hat{n}_{\mathbf{i}} = \sum_{\sigma} \hat{a}_{\mathbf{i}\sigma}^{\dagger} \hat{a}_{\mathbf{i}\sigma}$ and $\hat{\mathbf{S}}_{\mathbf{i}}$ are the local density and spin operators, respectively. Here $\langle \mathbf{i}, \mathbf{j} \rangle$ denotes nearest-neighbor (NN) lattice sites, t is the NN tunneling matrix element, J is the isotropic Heisenberg superexchange coupling and $\hat{\mathcal{P}}_G$ is the Gutzwiller projection operator which projects out all states with double occupancies. The bosonic $t - J$ model features both global SU(2) spin rotation symmetry and global U(1) particle number conservation symmetry, which we exploit in our numerical calculations [57].

In the following, we fix the total particle number $N = N_{\ell} - N_h$, where $N_{\ell} = L_x \times L_y$ is the number of lattice sites and N_h the total number of holes doped into the system (i.e., $\delta = N_h/N_{\ell}$). Moreover, we work in the regime with fully AFM spin-exchange interactions, $J > 0$, where the model exhibits a sign problem [39] and set $J = 1$.

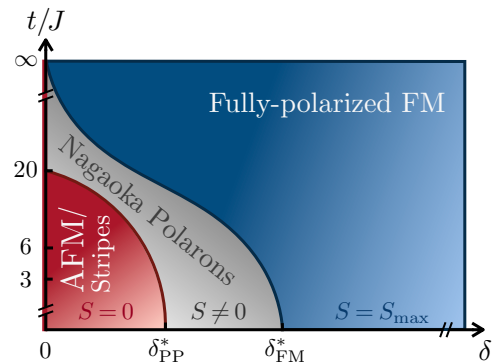


FIG. 1. Schematic $T = 0$ phase diagram of the AFM bosonic $t - J$ model indicating qualitatively different regions as a function of doping δ and interaction strength t/J . At half-filling (i.e., $\delta = 0$), the ground state is a long-range ordered Heisenberg AFM (red shaded region). At low doping, we also observe signatures of partially-filled stripes. As we increase doping, we identify a transition at $\delta = \delta_{\text{PP}}^*$ to a partially-polarized Nagaoka polaron regime (grey) and then to a fully-polarized FM phase (blue) at $\delta = \delta_{\text{FM}}^*$, characterized by total spin quantum numbers $S \neq 0$ and $S = S_{\text{max}}$, respectively. Along the y -axis, for $t/J \gtrsim 20$ ($t/J \rightarrow \infty$) previous numerical studies [58] have shown that a single dopant is sufficient to partially (or completely) polarize the system.

At half-filling ($\langle \hat{n}_{\mathbf{i}} \rangle = 1$), the kinetic motion of holes is frozen out and the ground state of the model, Eq. (1), is a long-range ordered Heisenberg AFM [59]. In this regime, the ground state at strong coupling is identical for both fermionic and bosonic Hubbard systems with AFM interactions. Moreover, in the case of only a single dopant, it can be shown analytically that the ground state remains independent of the underlying particle statistics. However, in the *finite doping* regime, i.e., where multiple holes are present, the distinction between fermionic and bosonic charge carriers becomes crucial. In this case, the system’s behavior is governed by the competition between the kinetic motion of holes and AFM superexchange interactions, leading to distinct correlated phases for fermionic and bosonic dopants.

Ground state correlations at finite doping.—We compute ground state properties of the doped AFM bosonic $t - J$ model, Eq. (1), via applying the DMRG algorithm [40–44] on finite cylinders [45] up to size $L_x \times L_y = 32 \times 6$ with open (periodic) boundaries along the x –(y)–direction(s). We explicitly perform calculations which implement both global $U(1)_N \otimes SU(2)_S$ and $U(1)_N \otimes U(1)_{S_z}$ symmetries to systematically verify the reliability of our results, and keep up to $\chi \sim 10,000$ SU(2) multiplets (i.e., equivalent to $\sim 30,000$ U(1) states) [57].

Kinetic magnetism and Nagaoka polarons.—To characterize the magnetic nature of the ground state at finite doping, we evaluate the total spin squared via summing over two-point spin–spin correlation functions:

$$\langle \hat{\mathbf{S}}^2 \rangle = \sum_{\mathbf{r}_1, \mathbf{r}_2=1}^{N_{\ell}} \langle \hat{\mathbf{S}}_{\mathbf{r}_1} \cdot \hat{\mathbf{S}}_{\mathbf{r}_2} \rangle. \quad (2)$$

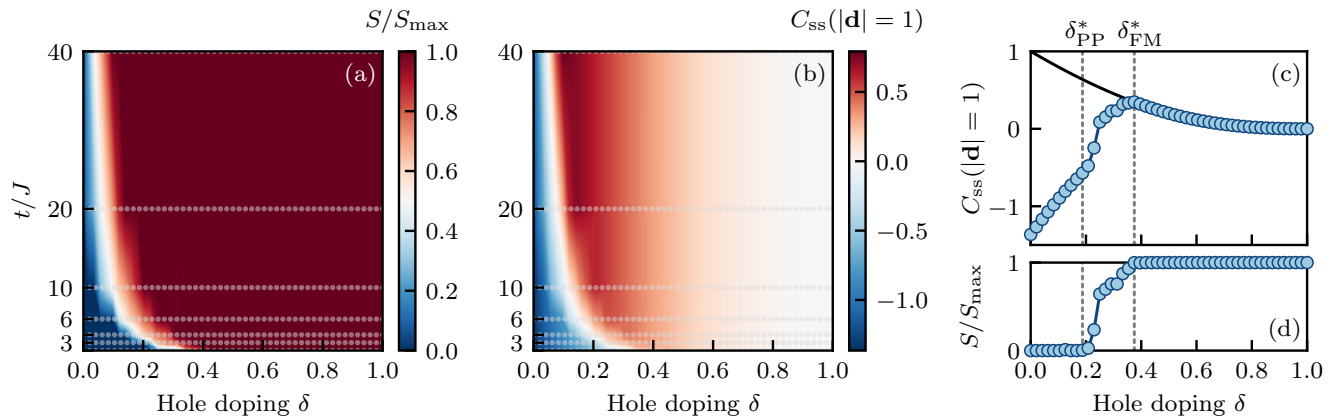


FIG. 2. Ground state phase diagram of the AFM bosonic $t-J$ model. (a) We compute the total spin quantum number S/S_{\max} as a function of hole doping δ and t/J obtained via DMRG simulations in the $S_z = 0$ symmetry sector (data points denoted by light gray circles). (b) A qualitatively similar phase diagram is obtained by analyzing the NN spin-spin correlation function $C_{\text{ss}}(|\mathbf{d}| = 1)$, also as a function of hole doping and t/J . In (c), (d) we show horizontal cuts through the data presented in (a), (b) for $t/J = 3$, illustrating a clear transition between the AFM, partially-polarized and fully-polarized FM regimes. The positions of the critical doping values δ_{PP}^* and δ_{FM}^* are denoted by vertical gray dashed lines. In the fully-polarized FM phase, i.e., for $\delta > \delta_{\text{FM}}^* \approx 0.38$, the NN correlations decay as $C_{\text{ss}} \propto (1 - |\delta|)^2$; the solid black line shows the correlations obtained from numerical simulations of a doped ferromagnet in the fully-polarized $S = S_{\max}$ symmetry sector. All DMRG calculations are performed on cylinders of size $L_x \times L_y = 16 \times 6$.

Computing the correlation functions numerically allows us to access the total spin S of the ground state via the relation $\langle \hat{\mathbf{S}}^2 \rangle = S(S + 1)$. A long-range SU(2) ferromagnet is characterized by maximum total spin quantum number $S_{\max} = (N_\ell - N_h)/2$. In Fig. 2(a), we plot the evolution of the total spin S/S_{\max} , normalized by its maximum value, as a function of doping for several values of t/J . We can clearly identify a regime close to half-filling ($\delta \approx 0$) where superexchange interactions dominate, resulting in a spin-singlet ground state with total spin $S = 0$.

As doping increases away from half-filling, the ground state transitions at $\delta = \delta_{\text{PP}}^*$ to a partially-polarized (PP) phase, characterized by total spin $S \neq 0$. At even higher doping, specifically for $\delta = \delta_{\text{FM}}^* > \delta_{\text{PP}}^*$, the system transitions into a fully-polarized FM phase where the total spin quantum number reaches its maximum value, $S = S_{\max}$. The fully-polarized FM phase remains stable even at very high doping, which distinguishes our findings from previous numerical studies of itinerant magnetism in geometrically frustrated fermionic systems [60].

To connect with possible experiments, we compute the connected spin-spin correlation function

$$C_{\text{ss}}(\mathbf{d}) = \frac{4}{\mathcal{N}_{\mathbf{d}}} \sum_{\mathbf{r}_1 - \mathbf{r}_2 = \mathbf{d}} \left(\langle \hat{\mathbf{S}}_{\mathbf{r}_1} \cdot \hat{\mathbf{S}}_{\mathbf{r}_2} \rangle - \langle \hat{\mathbf{S}}_{\mathbf{r}_2} \rangle \cdot \langle \hat{\mathbf{S}}_{\mathbf{r}_2} \rangle \right), \quad (3)$$

where the normalization factor $\mathcal{N}_{\mathbf{d}}$ denotes the number of lattice sites $\mathbf{r}_1, \mathbf{r}_2$ at a distance \mathbf{d} . In Fig. 2(b), we plot the NN spin-spin correlator $C_{\text{ss}}(|\mathbf{d}| = 1)$ as a function of doping δ for several ratios of t/J . At half-filling, superexchange interactions lead to a ground state characterized by strong NN AFM correlations (i.e., $C_{\text{ss}} < 0$). However,

as we increase the doping level, this negative correlation is suppressed due to motion of mobile bosonic holes in the system (see Fig. 2(c)). For $\delta < \delta_{\text{PP}}^*$, the ground state remains a total spin-singlet, as holes and spins interact in a way consistent with the formation of magnetic polarons or stripe-like order. Beyond the critical doping $\delta > \delta_{\text{PP}}^*$, as we enter the partially-polarized FM phase, each hole binds to a finite bubble of non-zero magnetization, forming Nagaoka polarons. Indeed, the NN correlations eventually turn ferromagnetic ($C_{\text{ss}} > 0$) and saturate beyond a critical doping value $\delta \gtrsim \delta_{\text{FM}}^*$, consistent with the picture of overlapping Nagaoka polarons driving a transition to a fully-polarized FM phase [51]. For $\delta > \delta_{\text{FM}}^*$, the NN correlations decay as $C_{\text{ss}} \propto (1 - |\delta|)^2$, as expected for a doped long-range SU(2) FM in this regime. Notably, the shift of δ_{FM}^* to lower doping with increasing t/J is consistent with the Nagaoka picture of a fully-polarized FM ground state emerging in the limit of infinitesimal positive doping as $t/J \rightarrow \infty$ [49].

Signatures of stripe order at low doping.—In addition to signatures of kinetic magnetism and Nagaoka polarons observed in the magnetic correlations at intermediate to high doping, we also identify evidence for the emergence of partially-filled stripes in the low-doping regime where the ground state is a total spin-singlet (i.e., $0 < \delta < \delta_{\text{PP}}^*$). To investigate this, we compute the normalized hole-hole correlation function

$$C_{\text{hh}}(\mathbf{r}_1, \mathbf{r}_2) = \langle \hat{n}_{\mathbf{r}_1}^h \hat{n}_{\mathbf{r}_2}^h \rangle / \langle \hat{n}_{\mathbf{r}_1}^h \rangle. \quad (4)$$

The correlator C_{hh} is suppressed if the presence of a hole at lattice site \mathbf{r}_1 makes it less likely to find a second hole

at site \mathbf{r}_2 , while C_{hh} is enhanced if it is more likely [10]. In Fig. 3, we plot C_{hh} together with the spin-spin correlations and hole density along the long (open) direction of the cylinder. In the ground state, we observe clear signatures of the formation of partially-filled stripes, indicated by (i) a periodic modulation of the hole density along the cylinder, and (ii) the appearance of AFM domain walls at positions of maximum hole density.

The hole-hole correlations (see Fig. 3(b)) indicate that individual bosonic dopants located within a single stripe repel one another along the short (periodic) direction of the cylinder, while there is no apparent spatial preference for two holes located within different stripes. This is in line with analogous charge correlations detected for fermionic stripes on finite cylinders [61], but stands in contrast to the emergence of tightly-bound hole pairs detected in previous numerical studies of paired phases in the 2D Fermi-Hubbard and $t - J$ models [61, 62].

Experimental realization.—Our study is motivated by recent advances in experimental platforms, e.g., bosonic quantum gas microscopes [28], Rydberg atom tweezer arrays [31] and ultracold polar molecules [30]. Here, we outline a scheme to adiabatically prepare strongly correlated many-body states of doped bosonic quantum antiferromagnets in ultracold atom experiments. This approach utilizes the unique advantages of ultracold atom quantum simulators, including their high degree of (local) control and tunability, combined with near perfect isolation from the surrounding environment.

For concreteness, we consider a quantum gas microscope of ^{87}Rb atoms in a 2D square lattice geometry, where the effective spin-1/2 degrees-of-freedom are encoded in a pair of hyperfine states, e.g., $|\downarrow\rangle \equiv |F = 1, m_F = -1\rangle$ and $|\uparrow\rangle \equiv |F = 2, m_F = 2\rangle$. Ultracold bosons in optical lattices are already an established platform for studying spin physics, offering insights into both equilibrium and out-of-equilibrium dynamics [63–71]. Crucially, ^{87}Rb atoms allow for the generation of strong, locally-programmable staggered fields, which can be employed to adiabatically prepare low-entropy states without crossing a phase transition, providing an additional advantage in realizing and exploring doped bosonic quantum magnets [28, 57].

Natively, ultracold bosons in optical lattices realize the spin-1/2 Bose-Hubbard model with (repulsive) on-site interactions $U_{\sigma\sigma'}$ between atoms and tunneling amplitude t . Working in sufficiently deep optical lattices allows us to reach the strong coupling limit ($U_{\sigma\sigma'} \gg t$), where the low-energy physics (i.e., without double occupancy) is effectively described by the bosonic $t - J$ model, Eq. (1), denoted here as $\hat{\mathcal{H}}(t, J)$, with *ferromagnetic* superexchange coupling $J = -4t^2/U < 0$ [72]. However, by leveraging the bounded nature of the spectrum in the low-energy sector, it is possible to “flip” the sign of the Hamiltonian in order to experimentally realize *antiferromagnetic* coupling between bosons [73–75]. This amounts to observing that the highest-energy eigenstate of the FM bosonic $t - J$

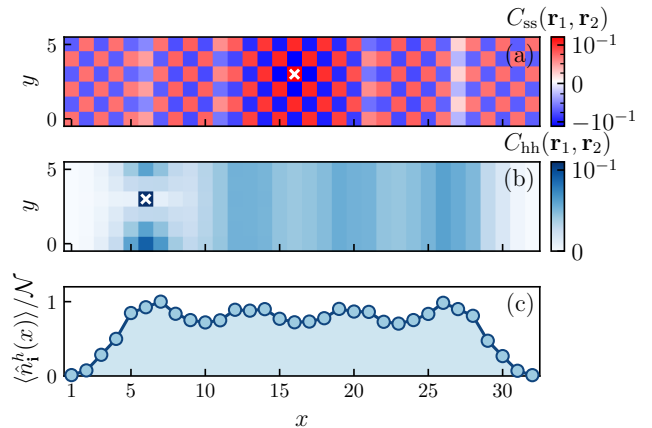


FIG. 3. Numerical DMRG simulations signaling the existence of stripe order at low doping. (a) We plot the connected spin-spin correlation function $C_{\text{ss}}(\mathbf{r}_1, \mathbf{r}_2)$ relative to the reference site $\mathbf{r}_1 = (16, 3)$ for a 32×6 cylinder at $t/J = 3$ and $\delta = 1/24$ in the $S = 0$ sector. Correlations are color coded using a symmetric logarithmic scale, with linear interpolation between -10^{-4} and 10^{-4} . Domain walls in the AFM background are indicated by neighboring pairs of lattice sites with like-signed correlations along the x -axis. (b) Normalized hole-hole correlation function $C_{\text{hh}}(\mathbf{r}_1, \mathbf{r}_2)$ with respect to the reference site $\mathbf{r}_1 = (6, 3)$. Within a stripe holes repel one another around the short (periodic) direction of the cylinder. (c) Mean hole density $\langle \hat{n}_i^h(x) \rangle = \sum_{y=1}^{L_y} \langle \hat{n}_i^h(x, y) \rangle / L_y$, normalized to unity, as a function of position along the long (open) x -direction of the cylinder. The density profile exhibits a periodic modulation, with hole rich regions corresponding to positions of AFM domain walls identified in (a). Reference sites are denoted by white crosses in (a) and (b).

model, $\hat{\mathcal{H}}(t, J)$, corresponds to the ground state of the AFM $t - J$ Hamiltonian $-\hat{\mathcal{H}}(t, J) = \hat{\mathcal{H}}(t, -J)$, where we have exploited the fact that on a bipartite lattice the sign of the tunneling matrix element t can be exchanged via a local gauge transformation $\hat{a}_{j\sigma} \rightarrow (-1)^j \hat{a}_{j\sigma}$, leaving the overall physics invariant [28].

In practice, implementing this scheme requires preparation of the highest excited eigenstate of the FM Hamiltonian $\hat{\mathcal{H}}(t, J)$ with high fidelity. At half-filling, this can be achieved by locally projecting a strong staggered field of strength $h_z \gg |J|$ onto the lattice, for which a 2D Néel state corresponds to the highest excited eigenstate of the system. Starting from this initial configuration, adiabatically ramping down the staggered field, i.e., $h_z \rightarrow 0$, then prepares the highest excited state of $\hat{\mathcal{H}}(t, J)$. To prepare ground states of doped bosonic quantum AFMs imposes further constraints on the state preparation protocol, additionally requiring that all holes in the system can be locally controlled [28]. In this way, striped ground states could also be directly prepared.

Outlook.—In this letter, we have analyzed the delicate interplay between kinetic and magnetic exchange mechanisms in the phase diagram of the doped AFM bosonic $t - J$ model. We identified a transition from AFM to FM ordered ground states as a function of both doping

and t/J , driven by the proliferation of Nagaoka polarons through the system. Additionally, we unveiled signatures of partially-filled stripe order in the low-doping regime, providing further evidence of a connection between our model and the strongly correlated phases of the fermionic Hubbard and $t - J$ models. Our results may be observed in state-of-the-art quantum simulation platforms, including quantum gas microscopes of ultracold bosonic atoms in optical lattices [28], Rydberg atom tweezer arrays [31] and systems of ultracold polar molecules [30].

Future work may include extending our results to finite temperatures ($T > 0$), thereby quantifying the effects of thermal fluctuations on the observed phase diagram of the doped AFM bosonic $t - J$ model, and exploring possible connections between low-temperature striped phases and the emergence of a pseudogap in doped bosonic systems [76–78]. From a practical perspective, it would also be interesting to investigate the influence of tunable hole-magnon couplings in the system [68, 79] (e.g., how these may modify spin-charge correlations in the finite doping regime), as well as the feasibility of utilizing tools including engineered dissipation [80–84], entropy redistribution [85, 86] and adiabatic cooling [28, 70, 87–91] to prepare strongly correlated many-body states of doped bosonic AFMs in ultracold atom experiments.

Note added.—During preparation of this manuscript, we became aware of a closely related work by Zhang *et al.* [92], in which they use DMRG to explore the phase diagram of the AFM bosonic $t - J$ model. In contrast to our study, the authors focus on finite cylinders of width $L_y = 4, 8$ using a combination of canonical ensemble and grand-canonical ensemble simulations, respectively, for which they report a pair-density wave with commensurate AFM order instead of the striped phase with incommensurate AFM order that we report in cylinders of width $L_y = 6$. Additionally, we note a slight difference in model parameters, with local density-density interaction $+\frac{3}{4}\hat{n}_i\hat{n}_j$ used in this work, compared to $-\frac{1}{4}\hat{n}_i\hat{n}_j$ in Ref. [92].

We wish to thank Tizian Blatz, Immanuel Bloch, Antoine Browaeys, Lukas Homeier, Hannah Lange, Sebastian Paeckel, Lode Pollet, Henning Schlömer, David Wei and Johannes Zeiher for valuable discussions. This research was supported by the Deutsche Forschungsgemeinschaft (DFG, German Research Foundation) under Germany’s Excellence Strategy EXC-2111 Grant No. 390814868 and the European Research Council (ERC) under the European Union’s Horizon 2020 research and innovation programme (Grant Agreement No. 948141), ERC Starting Grant SimUcQuam. T.J.H acknowledges funding by the Munich Quantum Valley (MQV) doctoral fellowship program, which is supported by the Bavarian state government with funds from the Hightech Agenda Bayern Plus. Numerical simulations were performed on the Arnold Sommerfeld Center for Theoretical Physics High-Performance Computing cluster and the KCS cluster at the Leibniz Supercomputing Center (LRZ).

* Tim.Harris@physik.uni-muenchen.de

† Fabian.Grusdt@physik.uni-muenchen.de

- [1] P. A. Lee, N. Nagaosa, and X.-G. Wen, Doping a Mott insulator: Physics of high-temperature superconductivity, *Rev. Mod. Phys.* **78**, 17 (2006).
- [2] V. J. Emery, Theory of high-Tc superconductivity in oxides, *Phys. Rev. Lett.* **58**, 2794 (1987).
- [3] F. C. Zhang and T. M. Rice, Effective Hamiltonian for the superconducting Cu oxides, *Phys. Rev. B* **37**, 3759 (1988).
- [4] B. Keimer, S. A. Kivelson, M. R. Norman, S. Uchida, and J. Zaanen, From quantum matter to high-temperature superconductivity in copper oxides, *Nature* **518**, 179 (2015).
- [5] Simons Collaboration on the Many-Electron Problem, J. P. F. LeBlanc, A. E. Antipov, F. Becca, I. W. Bulik, G. K.-L. Chan, C.-M. Chung, Y. Deng, M. Ferrero, T. M. Henderson, C. A. Jiménez-Hoyos, E. Kozik, X.-W. Liu, A. J. Millis, N. V. Prokof’ev, M. Qin, G. E. Scuseria, H. Shi, B. V. Svistunov, L. F. Tocchio, I. S. Tupitsyn, S. R. White, S. Zhang, B.-X. Zheng, Z. Zhu, and E. Gull, Solutions of the Two-Dimensional Hubbard Model: Benchmarks and Results from a Wide Range of Numerical Algorithms, *Phys. Rev. X* **5**, 041041 (2015).
- [6] Simons Collaboration on the Many-Electron Problem, M. Qin, C.-M. Chung, H. Shi, E. Vitali, C. Hubig, U. Schollwöck, S. R. White, and S. Zhang, Absence of Superconductivity in the Pure Two-Dimensional Hubbard Model, *Phys. Rev. X* **10**, 031016 (2020).
- [7] H. Xu, C.-M. Chung, M. Qin, U. Schollwöck, S. R. White, and S. Zhang, Coexistence of superconductivity with partially filled stripes in the Hubbard model, *Science* **384**, eadh7691 (2024).
- [8] E. Khatami and M. Rigol, Effect of particle statistics in strongly correlated two-dimensional Hubbard models, *Phys. Rev. A* **86**, 023633 (2012).
- [9] A. Bohrdt, L. Homeier, C. Reinmoser, E. Demler, and F. Grusdt, Exploration of doped quantum magnets with ultracold atoms, *Ann. Phys.* **435**, 168651 (2021).
- [10] S. Hirthe, T. Chalopin, D. Bourgund, P. Bojović, A. Bohrdt, E. Demler, F. Grusdt, I. Bloch, and T. A. Hilker, Magnetically mediated hole pairing in fermionic ladders of ultracold atoms, *Nature* **613**, 463 (2023).
- [11] D. Bourgund, T. Chalopin, P. Bojović, H. Schlömer, S. Wang, T. Franz, S. Hirthe, A. Bohrdt, F. Grusdt, I. Bloch, and T. A. Hilker, Formation of stripes in a mixed-dimensional cold-atom Fermi-Hubbard system (2023), [arXiv:2312.14156](https://arxiv.org/abs/2312.14156).
- [12] C. Gross and I. Bloch, Quantum simulations with ultracold atoms in optical lattices, *Science* **357**, 995 (2017).
- [13] A. Browaeys and T. Lahaye, Many-body physics with individually controlled Rydberg atoms, *Nat. Phys.* **16**, 132 (2020).
- [14] A. M. Kaufman and K.-K. Ni, Quantum science with optical tweezer arrays of ultracold atoms and molecules, *Nat. Phys.* **17**, 1324 (2021).
- [15] C. Weitenberg, M. Endres, J. F. Sherson, M. Cheneau, P. Schauß, T. Fukuhara, I. Bloch, and S. Kuhr, Single-spin addressing in an atomic Mott insulator, *Nature* **471**, 319 (2011).
- [16] J. Koepsell, S. Hirthe, D. Bourgund, P. Sompet, J. Vi-

- jayan, G. Salomon, C. Gross, and I. Bloch, Robust Bilayer Charge Pumping for Spin- and Density-Resolved Quantum Gas Microscopy, *Phys. Rev. Lett.* **125**, 010403 (2020).
- [17] G. Bornet, G. Emperauger, C. Chen, F. Machado, S. Chern, L. Leclerc, B. Gély, Y. T. Chew, D. Barredo, T. Lahaye, N. Y. Yao, and A. Browaeys, Enhancing a Many-Body Dipolar Rydberg Tweezer Array with Arbitrary Local Controls, *Phys. Rev. Lett.* **132**, 263601 (2024).
- [18] C. M. Holland, Y. Lu, S. J. Li, C. L. Welsh, and L. W. Cheuk, Demonstration of Erasure Conversion in a Molecular Tweezer Array (2024), [arXiv:2406.02391](https://arxiv.org/abs/2406.02391).
- [19] L. R. B. Picard, G. E. Patenotte, A. J. Park, S. F. Gebretsadkan, and K.-K. Ni, Site-Selective Preparation and Multistate Readout of Molecules in Optical Tweezers, *PRX Quantum* **5**, 020344 (2024).
- [20] D. K. Ruttley, A. Guttridge, T. R. Hepworth, and S. L. Cornish, Enhanced Quantum Control of Individual Ultracold Molecules Using Optical Tweezer Arrays, *PRX Quantum* **5**, 020333 (2024).
- [21] C. Gross and W. S. Bakr, Quantum gas microscopy for single atom and spin detection, *Nat. Phys.* **17**, 1316 (2021).
- [22] L. Christakis, J. S. Rosenberg, R. Raj, S. Chi, A. Morningstar, D. A. Huse, Z. Z. Yan, and W. S. Bakr, Probing site-resolved correlations in a spin system of ultracold molecules, *Nature* **614**, 64 (2023).
- [23] T. A. Hilker, G. Salomon, F. Grusdt, A. Omran, M. Boll, E. Demler, I. Bloch, and C. Gross, Revealing hidden antiferromagnetic correlations in doped Hubbard chains via string correlators, *Science* **357**, 484 (2017).
- [24] C. S. Chiu, G. Ji, A. Bohrdt, M. Xu, M. Knap, E. Demler, F. Grusdt, M. Greiner, and D. Greif, String patterns in the doped Hubbard model, *Science* **365**, 251 (2019).
- [25] J. Koepsell, D. Bourgund, P. Sompet, S. Hirthe, A. Bohrdt, Y. Wang, F. Grusdt, E. Demler, G. Salomon, C. Gross, and I. Bloch, Microscopic evolution of doped Mott insulators from polaronic metal to Fermi liquid, *Science* **374**, 82 (2021).
- [26] A. Impertro, Local Readout and Control of Current and Kinetic Energy Operators in Optical Lattices, *Phys. Rev. Lett.* **133**, 063401 (2024).
- [27] H. Schlömer, H. Lange, T. Franz, T. Chalopin, P. Bojović, S. Wang, I. Bloch, T. A. Hilker, F. Grusdt, and A. Bohrdt, Local control and mixed dimensions: Exploring high-temperature superconductivity in optical lattices (2024), [arXiv:2406.02551](https://arxiv.org/abs/2406.02551).
- [28] A. Bohrdt, D. Wei, D. Adler, K. Srakaew, S. Agrawal, P. Weckesser, I. Bloch, F. Grusdt, and J. Zeiher, Microscopy of bosonic charge carriers in staggered magnetic fields (2024), [arXiv:2410.19500](https://arxiv.org/abs/2410.19500).
- [29] A. V. Gorshkov, S. R. Manmana, G. Chen, J. Ye, E. Demler, M. D. Lukin, and A. M. Rey, Tunable Superfluidity and Quantum Magnetism with Ultracold Polar Molecules, *Phys. Rev. Lett.* **107**, 115301 (2011).
- [30] A. N. Carroll, H. Hirzler, C. Miller, D. Wellnitz, S. R. Muleady, J. Lin, K. P. Zamaraski, R. R. W. Wang, J. L. Bohn, A. M. Rey, and J. Ye, Observation of Generalized t-J Spin Dynamics with Tunable Dipolar Interactions (2024), [arXiv:2404.18916](https://arxiv.org/abs/2404.18916).
- [31] L. Homeier, T. J. Harris, T. Blatz, S. Geier, S. Holerith, U. Schollwöck, F. Grusdt, and A. Bohrdt, Antiferromagnetic Bosonic t-J Models and Their Quantum Simulation in Tweezer Arrays, *Phys. Rev. Lett.* **132**, 230401 (2024).
- [32] M. Boninsegni, Phase Separation in Mixtures of Hard Core Bosons, *Phys. Rev. Lett.* **87**, 087201 (2001).
- [33] M. Boninsegni, Phase separation and stripes in a boson version of a doped quantum antiferromagnet, *Phys. Rev. B* **65**, 134403 (2002).
- [34] J. Šmakov, C. D. Batista, and G. Ortiz, Stripes, Topological Order, and Deconfinement in a Planar $\text{t}\text{-J}\text{-z}$ Model, *Phys. Rev. Lett.* **93**, 067201 (2004).
- [35] M. Boninsegni and N. V. Prokof'ev, Phase diagram of an anisotropic bosonic $\text{t}\text{-J}$ model, *Phys. Rev. B* **77**, 092502 (2008).
- [36] K. Aoki, K. Sakakibara, I. Ichinose, and T. Matsui, Magnetic order, Bose-Einstein condensation, and superfluidity in a bosonic $\text{t}\text{-J}$ model of CP^1 spinons and doped Higgs holons, *Phys. Rev. B* **80**, 144510 (2009).
- [37] Y. Nakano, T. Ishima, N. Kobayashi, K. Sakakibara, I. Ichinose, and T. Matsui, Finite-temperature phase diagram of the three-dimensional hard-core bosonic $\text{t}\text{-J}$ model, *Phys. Rev. B* **83**, 235116 (2011).
- [38] Y. Nakano, T. Ishima, N. Kobayashi, T. Yamamoto, I. Ichinose, and T. Matsui, Finite-temperature phase diagram of two-component bosons in a cubic optical lattice: Three-dimensional $\text{t}\text{-J}$ model of hard-core bosons, *Phys. Rev. A* **85**, 023617 (2012).
- [39] J. Dicke, L. Rammelmüller, F. Grusdt, and L. Pollet, Phase diagram of mixed-dimensional anisotropic t-J models, *Phys. Rev. B* **107**, 075109 (2023).
- [40] U. Schollwöck, The density-matrix renormalization group in the age of matrix product states, *Ann. Phys.* **326**, 96 (2011).
- [41] U. Schollwöck, The density-matrix renormalization group, *Rev. Mod. Phys.* **77**, 259 (2005).
- [42] S. R. White, Density matrix formulation for quantum renormalization groups, *Phys. Rev. Lett.* **69**, 2863 (1992).
- [43] C. Hubig, *Symmetry-protected tensor networks*, Ph.D. thesis, LMU Munich, Faculty of Physics (2017).
- [44] C. Hubig, F. Lachenmaier, N.-O. Linden, T. Reinhard, L. Stenzel, A. Swoboda, M. Grunder, S. Mardazad, F. Pauw, and S. Paeckel, The SYTEN toolkit, <https://syten.eu/>.
- [45] E. Stoudenmire and S. R. White, Studying Two-Dimensional Systems with the Density Matrix Renormalization Group, *Annu. Rev. Condens. Matter Phys.* **3**, 111 (2012).
- [46] P. Corboz, S. R. White, G. Vidal, and M. Troyer, Stripes in the two-dimensional t-J model with infinite projected entangled-pair states, *Phys. Rev. B* **84**, 041108 (2011).
- [47] B.-X. Zheng, C.-M. Chung, P. Corboz, G. Ehlers, M.-P. Qin, R. M. Noack, H. Shi, S. R. White, S. Zhang, and G. K.-L. Chan, Stripe order in the underdoped region of the two-dimensional Hubbard model, *Science* **358**, 1155 (2017).
- [48] M. Qin, T. Schäfer, S. Andergassen, P. Corboz, and E. Gull, The Hubbard Model: A Computational Perspective, *Annu. Rev. Condens. Matter Phys.* **13**, 275 (2022).
- [49] Y. Nagaoka, Ferromagnetism in a Narrow, Almost Half-Filled s Band, *Phys. Rev.* **147**, 392 (1966).

- [50] M. L. Prichard, B. M. Spar, I. Morera, E. Demler, Z. Z. Yan, and W. S. Bakr, Directly imaging spin polarons in a kinetically frustrated Hubbard system, *Nature* **629**, 323 (2024).
- [51] M. Lebrat, M. Xu, L. H. Kendrick, A. Kale, Y. Gang, P. Seetharaman, I. Morera, E. Khatami, E. Demler, and M. Greiner, Observation of Nagaoka polarons in a Fermi–Hubbard quantum simulator, *Nature* **629**, 317 (2024).
- [52] J. P. Dehollain, U. Mukhopadhyay, V. P. Michal, Y. Wang, B. Wunsch, C. Reichl, W. Wegscheider, M. S. Rudner, E. Demler, and L. M. K. Vandersypen, Nagaoka ferromagnetism observed in a quantum dot plaquette, *Nature* **579**, 528 (2020).
- [53] Y. Tang, L. Li, T. Li, Y. Xu, S. Liu, K. Barnak, K. Watanabe, T. Taniguchi, A. H. MacDonald, J. Shan, and K. F. Mak, Simulation of Hubbard model physics in WSe₂/WS₂ moiré superlattices, *Nature* **579**, 353 (2020).
- [54] L. Ciorciaro, T. Smoleński, I. Morera, N. Kiper, S. Hiesland, M. Kroner, Y. Zhang, K. Watanabe, T. Taniguchi, E. Demler, and A. İmamoglu, Kinetic magnetism in triangular moiré materials, *Nature* **623**, 509 (2023).
- [55] Z. Tao, W. Zhao, B. Shen, T. Li, P. Knüppel, K. Watanabe, T. Taniguchi, J. Shan, and K. F. Mak, Observation of spin polarons in a frustrated moiré Hubbard system, *Nat. Phys.* **20**, 783 (2024).
- [56] R. Samajdar and R. N. Bhatt, Polaronic mechanism of Nagaoka ferromagnetism in Hubbard models, *Phys. Rev. B* **109**, 235128 (2024).
- [57] See Supplementary Materials for details regarding the DMRG implementation, experimental proposal and additional numerical results.
- [58] S. R. White and I. Affleck, Density matrix renormalization group analysis of the Nagaoka polaron in the two-dimensional $t\text{-}J$ model, *Phys. Rev. B* **64**, 024411 (2001).
- [59] P. Fazekas, *Lecture Notes on Electron Correlation and Magnetism* (WORLD SCIENTIFIC, 1999).
- [60] I. Morera and E. Demler, *Itinerant magnetism and magnetic polarons in the triangular lattice Hubbard model* (2024), arXiv:2402.14074.
- [61] T. Blatz, U. Schollwöck, F. Grusdt, and A. Bohrdt, *Two-dopant origin of competing stripe and pair formation in Hubbard and $t\text{-}J$ models* (2024), arXiv:2409.18131.
- [62] S. R. White and D. J. Scalapino, Hole and pair structures in the t - J model, *Phys. Rev. B* **55**, 6504 (1997).
- [63] S. Trotzky, P. Cheinet, S. Fölling, M. Feld, U. Schnorrberger, A. M. Rey, A. Polkovnikov, E. A. Demler, M. D. Lukin, and I. Bloch, Time-Resolved Observation and Control of Superexchange Interactions with Ultracold Atoms in Optical Lattices, *Science* **319**, 295 (2008).
- [64] J. Simon, W. S. Bakr, R. Ma, M. E. Tai, P. M. Preiss, and M. Greiner, Quantum simulation of antiferromagnetic spin chains in an optical lattice, *Nature* **472**, 307 (2011).
- [65] T. Fukuhara, P. Schauß, M. Endres, S. Hild, M. Cheneau, I. Bloch, and C. Gross, Microscopic observation of magnon bound states and their dynamics, *Nature* **502**, 76 (2013).
- [66] T. Fukuhara, A. Kantian, M. Endres, M. Cheneau, P. Schauß, S. Hild, D. Bellem, U. Schollwöck, T. Gimarchi, C. Gross, I. Bloch, and S. Kuhr, Quantum dynamics of a mobile spin impurity, *Nat. Phys.* **9**, 235 (2013).
- [67] S. Hild, T. Fukuhara, P. Schauß, J. Zeiher, M. Knapp, E. Demler, I. Bloch, and C. Gross, Far-from-Equilibrium Spin Transport in Heisenberg Quantum Magnets, *Phys. Rev. Lett.* **113**, 147205 (2014).
- [68] P. N. Jepsen, J. Amato-Grill, I. Dimitrova, W. W. Ho, E. Demler, and W. Ketterle, Spin transport in a tunable Heisenberg model realized with ultracold atoms, *Nature* **588**, 403 (2020).
- [69] P. N. Jepsen, W. W. Ho, J. Amato-Grill, I. Dimitrova, E. Demler, and W. Ketterle, Transverse Spin Dynamics in the Anisotropic Heisenberg Model Realized with Ultracold Atoms, *Phys. Rev. X* **11**, 041054 (2021).
- [70] H. Sun, B. Yang, H.-Y. Wang, Z.-Y. Zhou, G.-X. Su, H.-N. Dai, Z.-S. Yuan, and J.-W. Pan, Realization of a bosonic antiferromagnet, *Nat. Phys.* **17**, 990 (2021).
- [71] S. Kim, A. Lukin, M. Rispoli, M. E. Tai, A. M. Kaufman, P. Segura, Y. Li, J. Kwan, J. Léonard, B. Bakkali-Hassani, and M. Greiner, *Adiabatic State Preparation in a Quantum Ising Spin Chain* (2024), arXiv:2404.07481.
- [72] L.-M. Duan, E. Demler, and M. D. Lukin, Controlling Spin Exchange Interactions of Ultracold Atoms in Optical Lattices, *Phys. Rev. Lett.* **91**, 090402 (2003).
- [73] J. J. García-Ripoll, M. A. Martin-Delgado, and J. I. Cirac, Implementation of Spin Hamiltonians in Optical Lattices, *Phys. Rev. Lett.* **93**, 250405 (2004).
- [74] A. S. Sørensen, E. Altman, M. Gullans, J. V. Porto, M. D. Lukin, and E. Demler, Adiabatic preparation of many-body states in optical lattices, *Phys. Rev. A* **81**, 061603 (2010).
- [75] S. Braun, J. P. Ronzheimer, M. Schreiber, S. S. Hodgman, T. Rom, I. Bloch, and U. Schneider, Negative Absolute Temperature for Motional Degrees of Freedom, *Science* **339**, 52 (2013).
- [76] A. Wietek, Y.-Y. He, S. R. White, A. Georges, and E. M. Stoudenmire, Stripes, Antiferromagnetism, and the Pseudogap in the Doped Hubbard Model at Finite Temperature, *Phys. Rev. X* **11**, 031007 (2021).
- [77] F. Šimković, R. Rossi, A. Georges, and M. Ferrero, Origin and fate of the pseudogap in the doped Hubbard model, *Science* **385**, eade9194 (2024).
- [78] H. Schlömer, A. Bohrdt, and F. Grusdt, *Geometric fractionalized Fermi liquids: Hidden antiferromagnetism and pseudogap from fluctuating stripes* (2024), arXiv:2411.03419.
- [79] Y. K. Lee, M. Block, H. Lin, V. Fedoseev, P. J. D. Crowley, N. Y. Yao, and W. Ketterle, *Observation of spin squeezing with contact interactions in one- and three-dimensional easy-plane magnets* (2024), arXiv:2409.17398.
- [80] B. Kraus, H. P. Büchler, S. Diehl, A. Kantian, A. Micheli, and P. Zoller, Preparation of entangled states by quantum Markov processes, *Phys. Rev. A* **78**, 042307 (2008).
- [81] F. Verstraete, M. M. Wolf, and J. Ignacio Cirac, Quantum computation and quantum-state engineering driven by dissipation, *Nat. Phys.* **5**, 633 (2009).
- [82] A. J. Daley, Quantum trajectories and open many-body quantum systems, *Adv. Phys.* **63**, 77 (2014).
- [83] P. M. Harrington, E. J. Mueller, and K. W. Murch, Engineered dissipation for quantum information science, *Nat. Rev. Phys.* **4**, 660 (2022).

- [84] X. Mi, A. A. Michailidis, S. Shabani, K. C. Miao, P. V. Klimov, J. Lloyd, E. Rosenberg, R. Acharya, I. Aleiner, T. I. Andersen, M. Ansmann, F. Arute, K. Arya, A. Asfaw, J. Atalaya, J. C. Bardin, A. Bengtsson, G. Bortoli, A. Bourassa, J. Bovaird, L. Brill, M. Broughton, B. B. Buckley, D. A. Buell, T. Burger, B. Burkett, N. Bushnell, Z. Chen, B. Chiaro, D. Chik, C. Chou, J. Cogan, R. Collins, P. Conner, W. Courtney, A. L. Crook, B. Curtin, A. G. Dau, D. M. Debroy, A. Del Toro Barba, S. Demura, A. Di Paolo, I. K. Drozdov, A. Dunsworth, C. Erickson, L. Faoro, E. Farhi, R. Fatemi, V. S. Ferreira, L. F. Burgos, E. Forati, A. G. Fowler, B. Foxen, É. Genois, W. Giang, C. Gidney, D. Gilboa, M. Giustina, R. Gosula, J. A. Gross, S. Habegger, M. C. Hamilton, M. Hansen, M. P. Harrigan, S. D. Harrington, P. Heu, M. R. Hoffmann, S. Hong, T. Huang, A. Huff, W. J. Huggins, L. B. Ioffe, S. V. Isakov, J. Iveland, E. Jeffrey, Z. Jiang, C. Jones, P. Juhas, D. Kafri, K. Kechedzhi, T. Khattar, M. Khezri, M. Kieferová, S. Kim, A. Kitaev, A. R. Klots, A. N. Korotkov, F. Kostritsa, J. M. Kreikebaum, D. Landhuis, P. Laptev, K.-M. Lau, L. Laws, J. Lee, K. W. Lee, Y. D. Lensky, B. J. Lester, A. T. Lill, W. Liu, A. Locharla, F. D. Malone, O. Martin, J. R. McClean, M. McEwen, A. Mieszala, S. Montazeri, A. Morvan, R. Movassagh, W. Mroczkiewicz, M. Neeley, C. Neill, A. Nersisyan, M. Newman, J. H. Ng, A. Nguyen, M. Nguyen, M. Y. Niu, T. E. O'Brien, A. Opremcak, A. Petukhov, R. Potter, L. P. Pryadko, C. Quintana, C. Rocque, N. C. Rubin, N. Saei, D. Sank, K. Sankaragomathi, K. J. Satzinger, H. F. Schurkus, C. Schuster, M. J. Shearn, A. Shorter, N. Shuttly, V. Shvarts, J. Skrzynny, W. C. Smith, R. Somma, G. Sterling, D. Strain, M. Szalay, A. Torres, G. Vidal, B. Villalonga, C. V. Heidweiller, T. White, B. W. K. Woo, C. Xing, Z. J. Yao, P. Yeh, J. Yoo, G. Young, A. Zalcman, Y. Zhang, N. Zhu, N. Zobrist, H. Neven, R. Babbush, D. Bacon, S. Boixo, J. Hilton, E. Lucero, A. Megrant, J. Kelly, Y. Chen, P. Roushan, V. Smelyanskiy, and D. A. Abanin, Stable quantum-correlated many-body states through engineered dissipation, *Science* **383**, 1332 (2024).
- [85] A. Kantian, S. Langer, and A. J. Daley, Dynamical Disentangling and Cooling of Atoms in Bilayer Optical Lattices, *Phys. Rev. Lett.* **120**, 060401 (2018).
- [86] B. Yang, H. Sun, C.-J. Huang, H.-Y. Wang, Y. Deng, H.-N. Dai, Z.-S. Yuan, and J.-W. Pan, Cooling and entangling ultracold atoms in optical lattices, *Science* **369**, 550 (2020).
- [87] M. Lubasch, V. Murg, U. Schneider, J. I. Cirac, and M.-C. Bañuls, Adiabatic Preparation of a Heisenberg Antiferromagnet Using an Optical Superlattice, *Phys. Rev. Lett.* **107**, 165301 (2011).
- [88] J. Schachenmayer, D. M. Weld, H. Miyake, G. A. Siviloglou, W. Ketterle, and A. J. Daley, Adiabatic cooling of bosons in lattices to magnetically ordered quantum states, *Phys. Rev. A* **92**, 041602 (2015).
- [89] A. E. Mirasola, M. L. Wall, and K. R. A. Hazzard, Cooling fermions in an optical lattice by adiabatic demagnetization, *Phys. Rev. A* **98**, 033607 (2018).
- [90] A. Venegas-Gomez, J. Schachenmayer, A. S. Buyskikh, W. Ketterle, M. L. Chiofalo, and A. J. Daley, Adiabatic preparation of entangled, magnetically ordered states with cold bosons in optical lattices, *Quantum Sci. Technol.* **5**, 045013 (2020).
- [91] I. Dimitrova, S. Flannigan, Y. K. Lee, H. Lin, J. Amato-Grill, N. Jepsen, I. Čepaitė, A. J. Daley, and W. Ketterle, Many-body spin rotation by adiabatic passage in spin-1/2 XXZ chains of ultracold atoms, *Quantum Sci. Technol.* **8**, 035018 (2023).
- [92] H.-K. Zhang, J.-X. Zhang, J.-S. Xu, and Z.-Y. Weng, Quantum-interference-induced pairing in antiferromagnetic bosonic $\$t\$-\$J\$ model (2024), arXiv:2409.15424.$
- [93] D. Jaksch, C. Bruder, J. I. Cirac, C. W. Gardiner, and P. Zoller, Cold Bosonic Atoms in Optical Lattices, *Phys. Rev. Lett.* **81**, 3108 (1998).
- [94] A. Auerbach, *Interacting Electrons and Quantum Magnetism*, Graduate Texts in Contemporary Physics (Springer, New York, NY, 1994).
- [95] The other Néel state, $|\Psi_{\text{Néel}}\rangle = \prod_{i \in \mathcal{A}} \prod_{j \in \mathcal{B}} |\downarrow_i \uparrow_j\rangle$, with sublattices \mathcal{A} and \mathcal{B} reversed, corresponds to the ground state of the effective Hamiltonian $\mathcal{H}(\tau)$.
- [96] Y.-J. Xie, Bayesian learning for optimal control of quantum many-body states in optical lattices, *Phys. Rev. A* **106**, 013316 (2022).
- [97] T. Blatz, J. Kwan, J. Léonard, and A. Bohrdt, Bayesian Optimization for Robust State Preparation in Quantum Many-Body Systems, *Quantum* **8**, 1388 (2024).
- [98] C. Hubig, I. P. McCulloch, U. Schollwöck, and F. A. Wolf, Strictly single-site DMRG algorithm with subspace expansion, *Phys. Rev. B* **91**, 155115 (2015).
- [99] S. Singh, R. N. C. Pfeifer, and G. Vidal, Tensor network states and algorithms in the presence of a global U(1) symmetry, *Phys. Rev. B* **83**, 115125 (2011).
- [100] S. Singh and G. Vidal, Tensor network states and algorithms in the presence of a global SU(2) symmetry, *Phys. Rev. B* **86**, 195114 (2012).
- [101] A. Weichselbaum, Non-abelian symmetries in tensor networks: A quantum symmetry space approach, *Ann. Phys.* **327**, 2972 (2012).

Supplementary Materials: Kinetic magnetism and stripe order in the doped AFM bosonic $t - J$ model

In this supplementary material, we derive the relevant low-energy effective Hamiltonian that we investigate, i.e., the bosonic $t - J$ model, as well as provide further discussion regarding possible experimental realizations of our results in ultracold atom quantum simulators. Additionally, we outline important technical details related to the numerical methods utilized in our work, and provide further simulation results to support our conclusions.

I. The bosonic $t - J$ model

The bosonic $t - J$ model, Eq. (1), may be derived in the strong coupling limit (i.e., $U_{\sigma\sigma'} \gg t$) of the two-component (i.e., spin-1/2) Bose-Hubbard model, describing two species of bosons (e.g., encoded in two different hyperfine states of ^{87}Rb atoms) confined to the lowest Bloch band of an optical lattice [72, 93]:

$$\hat{H}_{\text{BH}} = \hat{H}_t + \hat{H}_U = - \sum_{\langle \mathbf{i}, \mathbf{j} \rangle} \sum_{\sigma} t_{\sigma} \left(\hat{a}_{\mathbf{i}\sigma}^{\dagger} \hat{a}_{\mathbf{j}\sigma} + \text{H.c.} \right) + \frac{1}{2} \sum_{\mathbf{i}, \sigma} U_{\sigma\sigma} \hat{n}_{\mathbf{i}\sigma} (\hat{n}_{\mathbf{i}\sigma} - 1) + U_{\uparrow\downarrow} \sum_{\mathbf{i}} \hat{n}_{\mathbf{i}\uparrow} \hat{n}_{\mathbf{i}\downarrow}, \quad (\text{S1})$$

where $\hat{a}_{\mathbf{i}\sigma}^{\dagger}$ ($\hat{a}_{\mathbf{i}\sigma}$) are the creation (annihilation) operators for a boson on lattice site \mathbf{i} in spin state $\sigma = \uparrow, \downarrow$; $\hat{n}_{\mathbf{i}\sigma} = \hat{a}_{\mathbf{i}\sigma}^{\dagger} \hat{a}_{\mathbf{i}\sigma}$ is the local density operator for spin- σ bosons, t_{σ} is the state-dependent NN tunneling matrix element and $U_{\sigma\sigma'}$ are the inter and intraspecies on-site interactions. Here $\langle \mathbf{i}, \mathbf{j} \rangle$ denotes pairs of nearest-neighbor (NN) lattice sites, and we note that the bosonic operators satisfy canonical commutation relations:

$$[\hat{a}_{\mathbf{i}\sigma}, \hat{a}_{\mathbf{j}\sigma'}] = [\hat{a}_{\mathbf{i}\sigma}^{\dagger}, \hat{a}_{\mathbf{j}\sigma'}^{\dagger}] = 0, \quad [\hat{a}_{\mathbf{i}\sigma}, \hat{a}_{\mathbf{j}\sigma'}^{\dagger}] = \delta_{\mathbf{ij}} \delta_{\sigma\sigma'}, \quad (\text{S2})$$

where $\delta_{\mathbf{ij}}, \delta_{\sigma\sigma'}$ denote Kronecker delta functions. In the strong coupling limit (i.e., $U_{\sigma\sigma'} \gg t$), performing a Schrieffer-Wolff transformation [59, 94] yields the following low-energy effective Hamiltonian, i.e., the bosonic $t - J$ model:

$$\begin{aligned} \hat{H}_{t-J} &= \hat{H}_t + \hat{H}_J + \hat{H}_{3\text{-site}} \\ &= - \sum_{\langle \mathbf{i}, \mathbf{j} \rangle} \sum_{\sigma} t_{\sigma} \hat{P}_G \left(\hat{a}_{\mathbf{i}\sigma}^{\dagger} \hat{a}_{\mathbf{j}\sigma} + \text{H.c.} \right) \hat{P}_G + \sum_{\langle \mathbf{i}, \mathbf{j} \rangle} \left(J_z \hat{S}_{\mathbf{i}}^z \hat{S}_{\mathbf{j}}^z + \frac{J_{\perp}}{2} \left(\hat{S}_{\mathbf{i}}^+ \hat{S}_{\mathbf{j}}^- + \text{H.c.} \right) + V \hat{n}_{\mathbf{i}} \hat{n}_{\mathbf{j}} - \frac{W}{2} \left(\hat{S}_{\mathbf{i}}^z \hat{n}_{\mathbf{j}} + \text{H.c.} \right) \right) \\ &\quad - \sum_{\langle \mathbf{i}, \mathbf{j}, \mathbf{k} \rangle} \sum_{\sigma} \left(\frac{t_{\sigma}^2}{U_{\uparrow\downarrow}} \hat{a}_{\mathbf{i}\sigma}^{\dagger} \hat{n}_{\mathbf{j}\bar{\sigma}} \hat{a}_{\mathbf{k}\sigma} + \frac{t_{\uparrow} t_{\downarrow}}{U_{\uparrow\downarrow}} \hat{a}_{\mathbf{i}\uparrow}^{\dagger} \hat{S}_{\mathbf{j}}^{\sigma} \hat{a}_{\mathbf{k}\sigma} + \frac{2t_{\sigma}^2}{U_{\sigma\sigma}} \hat{a}_{\mathbf{i}\sigma}^{\dagger} \hat{n}_{\mathbf{j}\sigma} \hat{a}_{\mathbf{k}\sigma} + \text{H.c.} \right) + \mathcal{O}(t^3/U^2), \end{aligned} \quad (\text{S3})$$

where \hat{P}_G is the Gutzwiller projection operator which restricts charge motion to the low-energy Hilbert space (i.e., without double occupancy), $\langle \mathbf{i}, \mathbf{j}, \mathbf{k} \rangle$ denotes adjacent pairs of NN lattice sites \mathbf{i}, \mathbf{j} and \mathbf{j}, \mathbf{k} with $\mathbf{i} \neq \mathbf{k}$, $\bar{\sigma}$ flips the spin ($\bar{\uparrow} = \downarrow$ and vice versa), $\hat{S}_{\mathbf{i}}^{\sigma} \equiv \hat{S}_{\mathbf{i}}^{\pm} (\hat{S}_{\mathbf{i}}^{\mp})$ for $\sigma = \uparrow (\downarrow)$, and we have introduced the Hamiltonian parameters [69, 72]:

$$\begin{aligned} J_z &= \frac{2(t_{\uparrow}^2 + t_{\downarrow}^2)}{U_{\uparrow\downarrow}} - \frac{4t_{\uparrow}^2}{U_{\uparrow\uparrow}} - \frac{4t_{\downarrow}^2}{U_{\downarrow\downarrow}}, \\ J_{\perp} &= -\frac{4t_{\uparrow} t_{\downarrow}}{U_{\uparrow\downarrow}}, \\ V &= -\frac{t_{\uparrow} t_{\downarrow}}{U_{\uparrow\downarrow}} - \frac{t_{\uparrow}^2}{U_{\uparrow\uparrow}} - \frac{t_{\downarrow}^2}{U_{\downarrow\downarrow}}, \\ W &= \frac{4t_{\uparrow}^2}{U_{\uparrow\uparrow}} - \frac{4t_{\downarrow}^2}{U_{\downarrow\downarrow}}. \end{aligned} \quad (\text{S4})$$

The Hamiltonian, Eq. (S3), describes hard-core bosonic particles tunneling on a lattice with NN magnetic interactions. The lower line describes second-order density-assisted and spin-flip-assisted NNN tunneling processes, respectively. In principle, both the sign and magnitude of the on-site interaction terms $U_{\sigma\sigma'}$ may be tuned via magnetic Feshbach resonance, as in Ref. [68]. However, for ^{87}Rb atoms such a Feshbach resonance is not easily accessible, and we recover the approximate SU(2) symmetric limit, i.e., taking $U_{\uparrow\uparrow} \approx U_{\downarrow\downarrow} \approx U_{\uparrow\downarrow} \equiv U$ and $t_{\uparrow} \approx t_{\downarrow} \equiv t$, and discarding three-site terms, which yields the bosonic $t - J$ Hamiltonian, Eq. (1), with $J = -4t^2/U < 0$, $V = 3J/4 < 0$ and $W = 0$.

II. Experimental realization in a bosonic quantum gas microscope

As outlined in the main text, the experimental setup we consider consists of a quantum gas microscope of ultracold bosonic ^{87}Rb atoms confined to a single plane of a 3D optical lattice, thereby realizing a 2D square lattice geometry. For each atom, we encode an effective spin-1/2 degree-of-freedom in a pair of hyperfine states, e.g., $|\downarrow\rangle \equiv |F=1, m_F=-1\rangle$ and $|\uparrow\rangle \equiv |F=2, m_F=2\rangle$. This setup naturally realizes the two-component Bose-Hubbard model, Eq. (S1), and in the strong coupling limit (i.e., $U_{\sigma\sigma'} \gg t$), the low-energy physics is well described by the bosonic $t-J$ model, Eq. (1), with *ferromagnetic* superexchange coupling $J = -4t^2/U < 0$ [72].

We propose to utilize metastable negative absolute-temperature states to engineer AFM couplings between bosons, following proposals in Refs. [73–75]. Specifically, we aim to prepare the highest-excited eigenstate of the FM bosonic $t-J$ model (see Sec. II. A for details), which on a bipartite lattice, e.g., the 2D square lattice, corresponds to the ground state of the AFM $t-J$ Hamiltonian. To see this, we note that on a bipartite lattice with sublattices \mathcal{A} and \mathcal{B} , the sign of the tunneling matrix element t can be exchanged via the local gauge transformation

$$\hat{a}_{\mathbf{j}\sigma} \rightarrow (-1)^{\mathbf{j}} \hat{a}_{\mathbf{j}\sigma} = \begin{cases} +\hat{a}_{\mathbf{j}\sigma}, & \mathbf{j} \in \mathcal{A}, \\ -\hat{a}_{\mathbf{j}\sigma}, & \mathbf{j} \in \mathcal{B}, \end{cases} \quad (\text{S5})$$

and likewise for $\hat{a}_{\mathbf{j}\sigma}^\dagger$. This transformation leaves the magnetic interaction term $\hat{\mathcal{H}}_J$ invariant, while mapping $\hat{\mathcal{H}}_t \rightarrow -\hat{\mathcal{H}}_t$. Therefore, when turning around the spectrum, it is only necessary to consider changing the sign of the spin-interaction in the FM Hamiltonian, $\hat{\mathcal{H}}_J \rightarrow -\hat{\mathcal{H}}_J$. Overall, we obtain that the high-energy physics of the FM bosonic $t-J$ model is described by $\hat{\mathcal{H}}'_{t-J} = -\hat{\mathcal{H}}_{t-J} = \hat{\mathcal{H}}_t - \hat{\mathcal{H}}_J$, which directly yields the AFM bosonic $t-J$ model introduced in Eq. (1).

A. Adiabatic state preparation scheme

We propose an adiabatic ramp protocol to prepare strongly correlated many-body states of doped bosonic quantum magnets. In this case, these states correspond to the highest-excited eigenstates of the FM bosonic $t-J$ Hamiltonian. The full state preparation protocol is outlined as follows:

1. Prepare a unit-filled spin-polarized Mott insulator of ^{87}Rb atoms, i.e., $|\Psi_{\text{Mott}}\rangle = \prod_{\mathbf{i}} |\downarrow\rangle_{\mathbf{i}}$, in a 2D square lattice.
2. Deterministically prepare the desired charge state (i.e., total N sector) via site-resolved addressing techniques.
3. We then apply strong local light-shifts on only a single sublattice, e.g., the \mathcal{A} sublattice, realizing the staggered field Hamiltonian $\hat{\mathcal{H}}_z(\tau) = h_z(\tau) \sum_{\mathbf{j}} (-1)^{\mathbf{j}} \hat{S}_{\mathbf{j}}^z$. The total effective Hamiltonian is then given by:

$$\hat{\mathcal{H}}(\tau) = \hat{\mathcal{H}}_{t-J} + \hat{\mathcal{H}}_z(\tau) = \hat{\mathcal{H}}_{t-J} + h_z(\tau) \sum_{\mathbf{j}} (-1)^{\mathbf{j}} \hat{S}_{\mathbf{j}}^z, \quad (\text{S6})$$

where $h_z(\tau)$ is the time-dependent field strength. The staggered field in Eq. (S6) may be realized (up to a global \hat{S}_z term) via locally programmable “anti-magic” differential light shifts available for ^{87}Rb [28].

4. Applying a global microwave π -pulse on the shifted $|\downarrow\rangle \leftrightarrow |\uparrow\rangle$ transition then resonantly transfers the remaining atoms on the \mathcal{A} sublattice from $|\downarrow\rangle \rightarrow |\uparrow\rangle$, preparing a product state in the desired total \hat{S}_z sector which is the highest-excited eigenstate of the effective Hamiltonian, Eq. (S6), for $h_z(\tau) > t \gg J$. For example, at half-filling, this protocol prepares the Néel state $|\Psi_{\text{Néel}}\rangle = \prod_{\mathbf{i} \in \mathcal{A}} \prod_{\mathbf{j} \in \mathcal{B}} |\uparrow_{\mathbf{i}} \downarrow_{\mathbf{j}}\rangle$ [95].
5. Finally, we adiabatically ramp down the staggered field, $h_z(\tau) \rightarrow 0$, to prepare the ground state $|\Psi_0\rangle$ of $\hat{\mathcal{H}}_{t-J}^{\text{AFM}}$. During this process, dopants are pinned by *anti-trapping potentials* in order to maximize the kinetic energy of the mobile bosonic holes. One example of a possible ramp profile, is given by an exponential ramp of the form $h_z(\tau) = h_0 e^{-\tau/T}$, parametrized by the total ramp time T . In the limit $T \rightarrow \infty$ the ramp is fully adiabatic.

Of course, the overall success of any (quasi-)adiabatic ramp protocol depends sensitively on the details of the low-energy eigenstates of the system. In particular, we note that the total ramp time T should scale as $T \propto 1/\Delta^2$ —with Δ the energy gap to the first excited state—in order to remain in the highest instantaneous eigenstate of the system. In this case, in the idealized SU(2)-invariant limit, there is a gap closing exactly at $h_z = 0$, which will result in a finite density of excitations in the final state for a finite preparation time. However, for sufficiently slow ramps, we expect this density to be small. A detailed investigation of realistic finite-time ramp protocols—which may be optimized via quantum control techniques [96, 97]—and the impact of experimental imperfections, including disorder, decoherence, state preparation and measurement (SPAM) errors, and thermal fluctuations, remains the subject of future work.

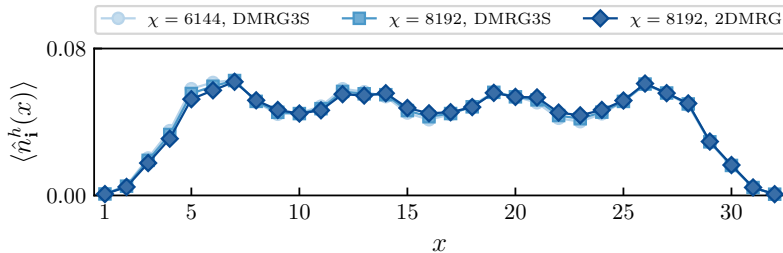


FIG. S1. We show the mean hole density profile $\langle n_1^h(x) \rangle = \sum_{y=1}^{L_y} \langle n_1^h(x, y) \rangle / L_y$ along the long (open) direction of the cylinder for the last three stages of our DMRG sweeping procedure, corresponding to the results shown in Fig. 3 of the main text. The lattice parameters are $L_x \times L_y = 32 \times 6$, $t/J = 3$ and $\delta = 1/24$ and the simulation is performed in the $S = 0$ symmetry sector using global $U(1)_N \otimes SU(2)_S$ symmetries. The maximum local MPS bond dimensions are given by $\chi = \{6144, 8192, 8192\}$, and we employ either strictly single-site (DMRG3S) or two-site (2DMRG) update schemes. The truncation error for the final stage (i.e., $\chi = 8192$, 2DMRG) is $\mathcal{T}(\epsilon) = 2.86 \times 10^{-6}$ with left-right imbalance $\mathcal{I} < 1\%$.

III. Numerical simulations using DMRG

All ground state calculations in this work were performed using the DMRG algorithm [40–42] in its matrix product state (MPS) formulation as implemented via the SYTEN toolkit [43, 44] on finite cylinders up to size $L_x \times L_y = 32 \times 6$ with open (periodic) boundaries along the x –(y –) direction(s) [45]. In particular, we utilize a combination of strictly single-site (DMRG3S) [98] and two-site (2DMRG) update schemes—scaling as $\mathcal{O}(\chi^3 dw)$ and $\mathcal{O}(\chi^3 d^2 w)$ respectively, where χ is the MPS bond dimension, d the dimension of the local Hilbert space and w is the matrix product operator (MPO) bond dimension—in order to ensure optimal convergence.

A. Implementation of non-abelian symmetries

The performance of the DMRG algorithm may be greatly enhanced by exploiting any available symmetries of the Hamiltonian under consideration. In addition to abelian symmetries that are available in standard open-source tensor network libraries, e.g., global $U(1)$ particle number $N = \sum_i \langle \hat{n}_i \rangle$ and magnetization $S_z = \sum_i \langle \hat{S}_i^z \rangle$ conservation [99], the SYTEN toolkit also allows for flexible implementation of non-abelian symmetries [100, 101], including global $SU(2)$ spin-rotation symmetry corresponding to conservation of the total spin quantum number S .

When utilizing non-abelian symmetries, the local MPS bond dimension χ_i required to faithfully represent a given quantum state is reduced to an effective bond dimension χ_i^* which counts multiplets only, i.e., groups of states each belonging to a given *irreducible representation* of the underlying non-abelian symmetry. The resulting reduction in the local bond dimension from $\chi_i \rightarrow \chi_i^*$ is given by a factor of $\mathcal{R} \sim 3^r$, where r is the *rank* of the underlying symmetry group, e.g., $\mathcal{R} \sim 3^{N-1}$ for $SU(N)$ which has rank $r = N - 1$ [101]. For more information about utilizing non-abelian symmetries in the context of tensor network calculations, we refer the interested reader to Refs. [100, 101].

From a numerical point of view, the reduction in the effective local bond dimension χ_i^* afforded by the use of $SU(2)$ spin-rotation symmetry in our calculations is incredibly valuable. In practice, for the Fermi/Bose-Hubbard and $t - J$ type Hamiltonians considered in this work, we find that this ratio is well aligned with the expected value $\mathcal{R} \approx 3$ when working in the $S = 0$ symmetry sector (i.e., total spin-singlet). Since the computational cost of the DMRG algorithm scales as $\mathcal{O}(\chi^3)$, we therefore expect a computational speed-up of $\mathcal{O}(3^3) \sim 30$ for a simulation of comparable accuracy.

There are some caveats to the practical benefits afforded by this approach, namely that when the total spin S of the ground state is changing as a function of a tunable system parameter (e.g., hole doping δ), then in order to correctly identify the ground state symmetry sector, (parallel) DMRG calculations must be performed in each of the accessible total S sectors, resulting in an additional computational overhead. Alternatively, the total spin quantum number can be determined from calculations implementing global $U(1)_N \otimes U(1)_{S_z}$ symmetries, as shown in Fig. 2 of the main text. In this work, we have explicitly performed calculations which implement both global $U(1)_N \otimes SU(2)_S$ and $U(1)_N \otimes U(1)_{S_z}$ symmetries, in order to systematically verify the reliability of our numerical results.

B. Analysis of convergence behavior

We initialize our simulations using a randomly generated state in the desired symmetry sector, i.e., (N, S_z) or (N, S) , before commencing our DMRG sweeps. We systematically increase the maximum bond dimension of our calculations

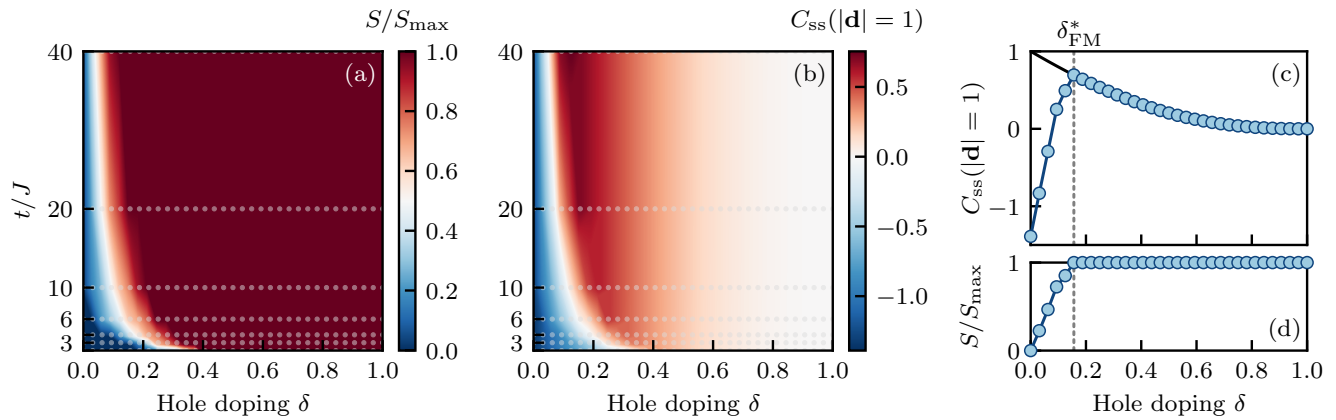


FIG. S2. Additional numerical results, as in Fig. 2 from the main text, obtained via DMRG calculations in the $S_z = 0$ symmetry sector performed on cylinders of size $L_x \times L_y = 16 \times 4$. Heatmaps showing (a) the total spin quantum number S/S_{\max} and (b) the NN spin–spin correlation function $C_{ss}(|\mathbf{d}| = 1)$ as a function of hole doping δ and t/J , respectively (data points are denoted by light gray circles). In (c), (d) we show horizontal cuts through the data in (a), (b) for $t/J = 20$. For $t/J = 20$, $\delta_{\text{PP}}^* \approx 0$ and the system is immediately partially polarized upon doping, as indicated by the departure from a spin-singlet ground state for $\delta \neq 0$. In the fully-polarized FM phase, i.e., $\delta > \delta_{\text{FM}}^* \approx 0.16$, the NN correlations decay as $C_{ss} \propto (1 - |\delta|)^2$, consistent with the correlations obtained from numerical simulations of a doped ferromagnet in the $S = S_{\max}$ symmetry sector (solid black line).

until convergence is reached. For the ground state calculations shown in the main text, we utilized bond dimensions up to $\chi = 10,240$ (equivalent to $\chi \sim 30,000$ U(1) symmetric states for calculations using SU(2) spin-rotation symmetry) and obtain typical truncation errors $\mathcal{T}(\epsilon) \sim \mathcal{O}(10^{-7})$ and $\mathcal{T}(\epsilon) \sim \mathcal{O}(10^{-6})$ for $L_y = 4$ and $L_y = 6$ width cylinders, respectively. To further ensure optimal convergence, we monitor local one- and two-body observables, including the local hole density, spin expectation values, hole–hole and spin–spin correlation functions.

In Fig. S1, we show the mean hole density $\langle n_i^h(x) \rangle = \sum_{y=1}^{L_y} \langle n_i^h(x, y) \rangle / L_y$ corresponding to the last three DMRG stages used to obtain the numerical results presented in Fig. 3 of the main text. The hole density serves as a sensitive probe for numerical convergence, as slight real-space perturbations to the density profile are typically associated with very small energy cost. Moreover, the sweeping nature of the DMRG algorithm itself means that it is generally difficult to obtain a symmetric profile. We observe that in Fig. S1, the hole density is slightly asymmetric for $\chi = 6144$, but symmetric and almost indistinguishable for the final two stages with $\chi = 8192$, indicating that the final state is likely well converged. To quantify the asymmetry, we compute the imbalance $\mathcal{I} = (N_h^L - N_h^R) / N_h$, defined as the particle number difference between the left (L) and right (R) sides of the system, where $N_h^\sigma = \sum_{i \in \sigma} \langle \hat{n}_i^h \rangle$ for $\sigma = L, R$. We find that in the final DMRG stage, the hole density profile is indeed well converged, with left-right asymmetry $\mathcal{I} < 1\%$.

C. Additional numerical results

In Fig. S2, we show additional numerical results for the total spin quantum number and local spin–spin correlations obtained on cylinders of size $L_x \times L_y = 16 \times 4$. We observe a qualitatively similar phase diagram for these calculations, as in Fig. 2 of the main text, obtained for width-6 cylinders of size $L_x \times L_y = 16 \times 6$. This indicates that the phase diagram we obtain is not strongly influenced by finite-size effects.